J. Fluid Mech. (1982), *vol.* 121, *pp.* 27–42
Printed in Great Britain

The viscous spreading of plane and axisymmetric gravity currents

By N. DIDDEN AND T. MAXWORTHY

Departments of Mechanical and Aerospace Engineering, University of Southern California, Los Angeles, California 90007

(Received 12 February 1981 and in revised form 7 July 1981)

Measurements of the spreading rates of gravity-driven currents at both the surface and the bottom of a fluid layer of different density are reported. For the case of a constant inflow rate the spreading relations are derived by estimating the order of magnitude of the forces involved. After an initial balance between gravity and inertia forces the final spreading phase is governed by the balance between gravity and viscous forces. For the latter flow regime, measurements in plane and axisymmetric flow geometries agree well with the spreading relations for gravity currents with a no-slip boundary. The proportionality factor, which is not predicted from this model, is then determined from the measurements and a good agreement is found with the theoretical value derived in the accompanying paper by Huppert (1982).

1. Introduction

The inflow of one fluid into another fluid of different density is encountered in many geophysical and industrial flow situations. Whenever light fluid discharges into heavier fluid it rises to the surface and then spreads along the surface, driven by the horizontal pressure gradient due to the density difference. Similarly, the discharge of heavy fluid results in a current spreading on the bottom of a light fluid reservoir. The horizontal spreading of both surface and bottom currents is governed by an interplay between gravity, inertia and viscous forces. In what follows we neglect the effect of Coriolis forces, i.e. currents considered here are related to small-scale atmospheric and oceanic fronts of large Rossby number only. Some examples are sea breeze fronts (Simpson, Mansfield & Milford 1977), plume fronts from river inflows into the ocean (Garvine & Monk 1974) and estuarine fronts generated by tidal mixing in shoaling areas (Klemas & Polis 1977). Industrial problems connected with gravity-driven currents arise from warm-water discharge from power plants, the spreading of oil on the sea surface (Hoult 1972), and the discharge of effluent into rivers, lakes and coastal seas.

In our study we consider one of the most basic aspects of small-scale frontal dynamics, that is the spreading rate and the types of force balance that characterize this spreading. Gravity currents, set up by releasing a constant volume of fluid of density ρ_1 into ambient fluid of density ρ_0 (with $\Delta\rho = |\rho_1 - \rho_0|$), have been studied by various experimenters. Here we study another important and related case, the release of current fluid at a constant flow rate Q. In both cases, as argued by Fay (1969), the driving gravity force is initially balanced by inertia forces, and the internal Froude number $Fr = U/(g'h)^{\frac{1}{2}}$ is constant (U is the spreading velocity of the front, $g' = g\Delta\rho/\rho_0$ is the reduced gravity, g is the acceleration due to gravity, and h is the current thickness). For this flow regime Hoult (1972) measured a constant Froude number $Fr = 1{\cdot}18$ for the spreading of oil on water. Huppert & Simpson (1980) showed

for bottom gravity currents with constant volume that for an initial depth ratio $h/H > 0{\cdot}1$ (H is the ambient fluid depth) the gravity–inertia regime is preceded by a slumping regime, in which the Froude number increases as the depth ratio decreases. This dependence of the Froude number on the depth ratio h/H has been analysed theoretically by Benjamin (1968) with some success. The gravity–inertia balance is maintained as long as the inertia force is large compared with the total viscous drag resulting from interfacial shear stress between the current and the ambient fluid or from bottom shear stress. As time progresses, the viscous force becomes larger than the inertia force, and finally a second flow regime is established, in which the gravity force is balanced by the viscous drag. To our knowledge, measurements for this gravity–viscous regime have been reported only by Hoult (1972) for a constant-volume release of oil spreading on water and by Maxworthy (1972) for an internal intrusion into a stratified fluid, released at a constant flow rate. In Hoult's case, because of the high oil viscosity he was able to assume a slug flow (i.e. a constant velocity in the oil layer) and to estimate the viscous stress at the interface considering only the boundary-layer growth in the water below the oil layer. Although in Hoult's model the condition at the current head is somewhat unsatisfactory, as discussed by Huppert & Simpson (1980), the spreading rate derived for the gravity–viscous balance of this slug flow agreed well with Hoult's experiments. In the case considered here, however, the density difference between the current fluid and the ambient fluid is due to differences in salinity or temperature, the viscosity difference is negligible, and the slug-flow assumption cannot be made *a priori*. Instead of a boundary layer in the ambient fluid only, a shear layer develops at the interface between both fluids. Furthermore, one expects the total viscous drag to be different for the surface and bottom currents since the surface should be a stress-free boundary† whereas at the bottom the no-slip condition applies.

In the present paper we consider the spreading of gravity currents supplied with a constant flow rate from either a line source or a point source, resulting, respectively in a plane flow with a straight front or an axisymmetric flow with a circular front. For these conditions we derive the spreading relations for the gravity–inertia and the gravity–viscous regimes (§2). The experimental setups for the plane and axisymmetric gravity currents are described in §3, and measurements of the spreading rate in the gravity–viscous regime are presented in §4 for comparison with the analytical results.

2. The spreading relations

We consider a gravity current of density ρ_1 and thickness $h(x, t)$ at the surface or the bottom of ambient fluid of density ρ_0 and depth $H \gg h$ (figure 1). The current is supplied with a constant flow rate Q (cm^3/s) from a source at the origin of the co-ordinate system. In the case of a plane current the source extends perpendicular to the (x, z)-plane over a width w (in the experiments the channel width) and the flow rate per unit width is $\bar{Q} = Q/w$. Alternatively, an axisymmetric gravity current is formed if fluid is released from an axisymmetric source and allowed to spread radially in the horizontal direction. The current with a circular front of radius R will be described in a co-ordinate system with x and z now being the radial and axial cylinder co-ordinates respectively. In both cases the characteristic time-dependent scaling variables are the current thickness $h_0(t)$ at the source, the front-velocity $U(t)$, the current length $L(t)$ and radius $R(t)$. The independent flow parameters are the density difference $\Delta\rho$ (or the reduced gravity $g' = g\Delta\rho/\rho_1$) and the flow rate Q.

† See §4 for further comments on this condition.

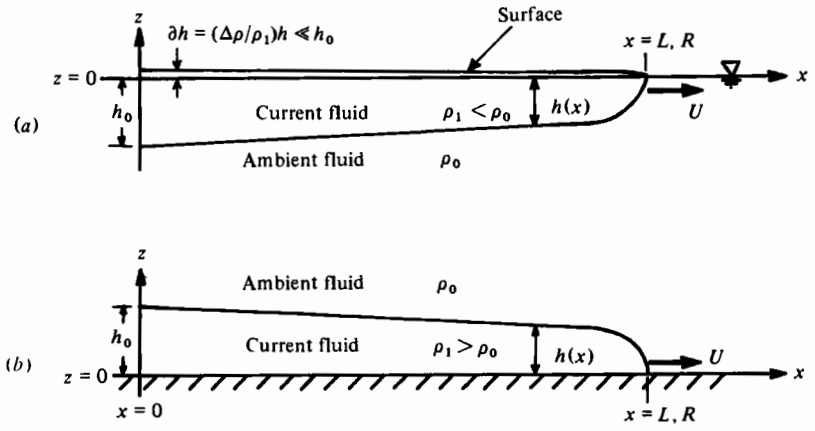

FIGURE 1. Parameters of the plane surface current (*a*) and bottom current (*b*). For the axisymmetric current x and z are radial and axial cylinder co-ordinates. L = current length (plane current), R = current radius (axisymmetric current).

For an oil current of constant volume spreading on a water surface Hoult (1972) showed that similarity solutions of the flow field exist for both the regime of gravity–inertia balance and for the balance of gravity and viscous forces. This encourages us to assume similarity also for a gravity current of fluid miscible with the ambient fluid and supplied with a constant flow rate Q. In this case the spreading relations, except for the proportionality factor, can be derived by simply estimating the order of magnitude of the forces acting on the current. The full similarity solution, including the proportionality factor, can only be derived by solving the governing differential equations, which is done in an accompanying paper by Huppert (1982), who calculates the values of the factor of proportionality. Here the factor is determined experimentally.

Since in the following we neglect mixing across the interface between the two fluids of different densities, the orders of magnitude (henceforth denoted by $\sim$) of the fluid volume for the plane and axisymmetric currents respectively are

$$\bar{Q}t \sim h_0 L, \quad \text{(plane)}, \tag{1a}$$

$$Qt \sim h_0 R^2, \quad \text{(axisymmetric)}, \tag{1b}$$

where t is the time from initiation of the flow. In hydrostatic balance the surface of the surface current is elevated a height $\delta h = h\Delta\rho/\rho_1$ above the surface of the ambient fluid. From vertical integration of the hydrostatic equation the pressure distribution in the current is easily derived. The driving horizontal pressure gradient for both surface currents and bottom currents is then

$$\partial p/\partial x = \Delta\rho g \partial h/\partial x. \tag{2}$$

It should be noted that the pressure gradient and thus the horizontal acceleration in the current are constant across the current depth. The orders of magnitude of the horizontal gravity force derived from integrating (2) over the current volume are

$$F_g \sim \Delta\rho g h_0^2 w \sim \Delta\rho g \bar{Q}^2 t^2 w/L^2 \quad \text{(plane)}, \tag{3a}$$

$$F_g \sim \Delta\rho g h_0^2 R \sim \Delta\rho g Q^2 t^2/R^3 \quad \text{(axisymmetric)}. \tag{3b}$$

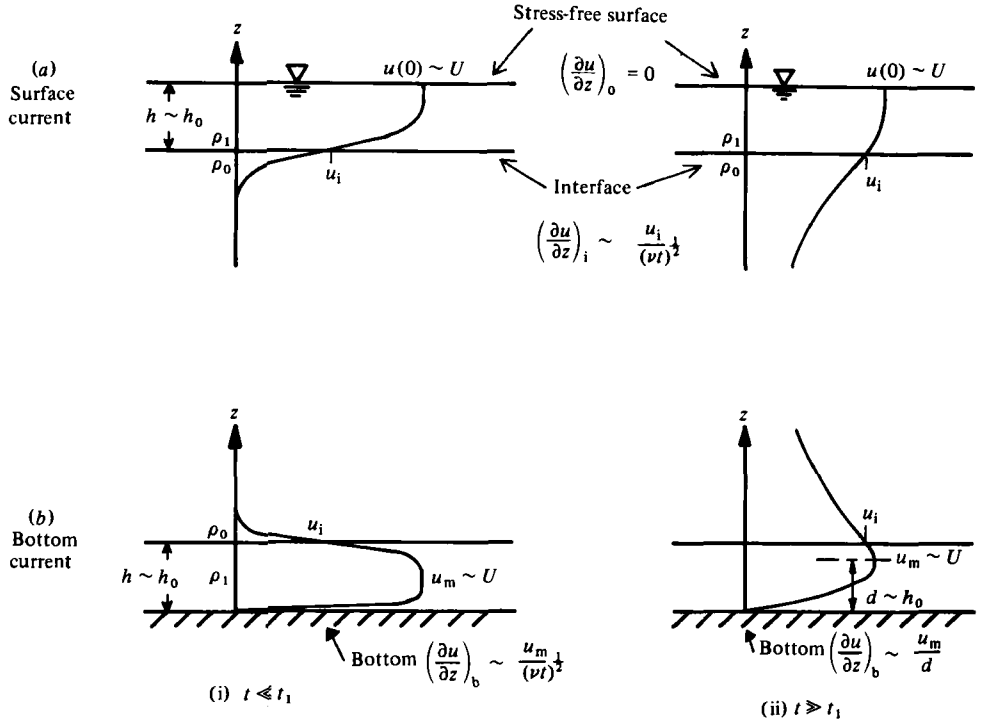

FIGURE 2. Velocity profiles $u(z)$ schematically for $t \ll t_1$ and $t \gg t_1$. At $t = t_1 \sim h_0^2/\nu$ the boundary-layer thickness and the shear-layer thickness $\delta \sim (\nu t)^{\frac{1}{2}}$ are of the same order of magnitude as the current thickness h_0.

The current is driven by gravity exclusively if the inertia of the discharging fluid does not exceed the gravity force. This condition can be expressed quantitatively by only considering flows that are subcritical, i.e. the discharge Froude number at the source inlet $Fr_i = U_i/(g'h_i)^{\frac{1}{2}}$ must be of order unity or smaller (U_i is the horizontal inflow velocity and h_i the depth of the inlet opening). The other alternative, which we do not consider, is a horizontally discharging buoyant jet with supercritical Froude number $Fr_i > O(1)$, for which the initial force balance would be between a driving inertia and a retarding viscous force. In this case the main effect of gravity is to suppress vertical mixing and to enhance lateral spreading (McGuirk & Rodi 1979). For our subcritical flow, however, inertia is a retarding force and balances the driving gravity force as long as the viscous drag can be neglected. The order of magnitude of the inertia force is, using (1) and $U \sim L/t$ or R/t,

$$F_i \sim \rho_1 U^2 h_0 w \sim \rho_1 \tilde{Q} L w/t \quad \text{(plane)}, \tag{4a}$$

$$F_i \sim \rho_1 U^2 h_0 R \sim \rho_1 Q R/t \quad \text{(axisymmetric)}. \tag{4b}$$

In order to estimate the viscous drag of the gravity current we model the flow field as shown in figure 2. The difference between the dynamic viscosities μ of both fluids is assumed to be small. Furthermore, we are concerned with small density differences $\Delta\rho \ll \rho_1$ only, and thus the kinematic viscosities ν of both fluids are comparable as well. We first consider the initial stages of the motion (figures 2*a*, *b* (i)). Since the horizontal acceleration due to gravity is independent of z (see (2)) the

velocity gradient $\partial u/\partial z$ in the current is initially zero. At the interface a shear layer of thickness $\delta \sim (\nu t)^{\frac{1}{2}}$ develops, with a viscous stress given approximately by $\tau \sim \mu(\partial u/\partial z)_i \sim \mu U/(\nu t)^{\frac{1}{2}}$. For the surface current the condition of no stress ($\partial u/\partial z = 0$) applies at the free surface, whereas for the bottom current the bottom stress $\tau_b \sim \mu U/(\nu t)^{\frac{1}{2}}$, in a boundary layer of thickness $\delta \sim (\nu t)^{\frac{1}{2}}$, also contributes to the total viscous drag. Since the bottom stress is of the same order of magnitude as the interfacial stress at this initial stage of the motion, the order of magnitude of the total viscous stress for the bottom and the surface current is

$$\tau \sim \mu U/(\nu t)^{\frac{1}{2}}. \tag{5}$$

The above relations are valid as long as the shear-layer thickness and the boundary-layer thickness are smaller than the current thickness, i.e. for $\delta < h_0$ or $t < t_1 \sim h_0^2/\nu$.

At later times, when $t > t_1$, the further time dependence has to be considered separately for the surface current and the bottom current owing to the different boundary conditions. First we note that since the driving force for the motion resides within the gravity current the maximum velocity must also exist there (figures 2*a*, *b* (ii)). For the surface current with a stress-free boundary the maximum velocity must be located at the surface, that is the velocity at the surface is $u_s \sim U$. Using the similarity assumption with vertical scales h_0 and $\delta = (\nu t)^{\frac{1}{2}}$ in the current and the ambient fluid respectively, and with corresponding velocity differences $u_s - u_i$ and $u_i - 0$ (see figure 2*a* (ii)), we find the velocity u_i at the interface from the condition that the shear stress is continuous across the interface:

$$\tau_i = \mu(\partial u/\partial z)_i = c_1\mu(u_s - u_i)/h_0 = c_2\mu u_i/\delta.$$

This results in

$$u_i = u_s(1 + c_3 h_0/\delta)^{-1}.$$

Here c_1, c_2 and c_3 are constants of order unity. For $\delta \gg h_0$ or $t \gg t_1 \sim h_0^2/\nu$ the value of the term in parentheses approaches unity, so that the velocity gradient across the current depth becomes small, although it must remain non-zero in order to satisfy the stress condition at the interface. Neglecting this weak dependence of the bracket term for $t \gg t_1$, we obtain $u_i \sim u_s$. Then the shear stress of the surface current again is given by (5), and the total viscous drag is

$$F_v \sim \mu ULw/(\nu t)^{\frac{1}{2}} \quad \text{(plane)}, \tag{6a}$$

$$F_v \sim \mu UR^2/(\nu t)^{\frac{1}{2}} \quad \text{(axisymmetric)}, \tag{6b}$$

with different constants of proportionality for $t \ll t_1$ and $t \gg t_1$. The same relation derived from (5) is valid for the bottom current at $t \ll t_1$.

We now consider the bottom current at $t \gg t_1$ (figure 2*b* (ii)). Since the ambient fluid is always driven by the current, the maximum velocity u_m in the vertical profile is located within the current, say at $z = d < h_0$. Assuming that for $t \gg t_1$ the vertical profile in the current depends on the similarity variable z/h_0 only, the bottom stress is given by

$$\tau_b \sim \mu u_m/d \sim \mu U/h_0.$$

The interfacial stress $\tau_i \sim \mu U/(\nu t)^{\frac{1}{2}}$ continues to decrease, and for $(\nu t)^{\frac{1}{2}} \gg h_0$ or $t \gg t_1$ it becomes small compared with the bottom stress. Thus the total viscous drag of the bottom current for $t \gg t_1$ is determined by the bottom stress only:

$$F_v \sim \mu ULw/h_0 \sim \mu L^2 w/h_0 t \quad \text{(plane)}, \tag{7a}$$

$$F_v \sim \mu UR^2/h_0 \sim \mu R^3/h_0 t \quad \text{(axisymmetric)}. \tag{7b}$$

For the plane-current experiments in a channel of finite width, w, the viscous stress at the sidewalls should be taken into account as well.† The sidewall stress in the developing boundary layer, with y being the transverse co-ordinate, is of order $\tau_w = \mu\partial u/\partial y \sim \mu U(\nu t)^{-\frac{1}{2}}$ for $t < t_2 = (\frac{1}{2}w)^2/\nu$. Our measurements were performed at $t < t_2$, and thus the viscous drag from both sidewalls is $F_{vw} \sim 2\mu U(\nu t)^{-\frac{1}{2}} h_0 L$. Comparison with (7$a$) gives the total viscous drag for the no-slip boundary current:

$$F'_v = F_v + F_{vw} = F_v(1 + 2ch_0^2(t)/w(\nu t)^{\frac{1}{2}}),$$

with an unknown constant $c = O(1)$. The correction factor $\alpha = 1 + 2ch_0^2/w(\nu t)^{\frac{1}{2}}$ for a finite-width channel is weakly time-dependent. In our further analysis we assume $w \gg h_0$ and drop the correction factor, but further comments will be made in the discussion of the experimental results in §4.

Comparisons of (4) with (6) and (7) shows, that the viscous drag is negligible compared with the inertia force for $(\nu t)^{\frac{1}{2}} \ll h_0$, that is for $t \ll t_1$. Accordingly, as long as the shear-layer thickness and the boundary-layer thickness are small compared with the current thickness h_0 the driving gravity force can only be balanced by the inertial force. For this gravity–inertia regime the spreading relation derived by equating (3) and (4) for $t \ll t_1$ is

$$L \sim (g'\tilde{Q})^{\frac{1}{3}} t, \quad h_0 \sim (\tilde{Q}^2/g')^{\frac{1}{3}} \quad \text{(plane)}, \tag{8a}$$

$$R \sim (g'Q)^{\frac{1}{4}} t^{\frac{3}{4}}, \quad h_0 \sim (Q/g')^{\frac{1}{2}} t^{-\frac{1}{2}} \quad \text{(axisymmetric)}. \tag{8b}$$

The 'transition time' t_1, at which inertia and viscous forces are of the same order of magnitude, is

$$t_1 = (\tilde{Q}^4/g'^2\nu^3)^{\frac{1}{5}} \quad \text{(plane)}, \tag{9a}$$

$$t_1 = (Q/g'\nu)^{\frac{1}{2}} \quad \text{(axisymmetric)}. \tag{9b}$$

For $t \gg t_1$, the viscous drag becomes the dominant retarding force balancing the gravity force. From (3) and (6) we find the spreading relations for the *surface current* in this gravity–viscus regime:

$$L \sim (g'\tilde{Q}^2/\nu^{\frac{1}{2}})^{\frac{1}{8}} t^{\frac{7}{8}}, \quad h_0 \sim (\nu^{\frac{1}{2}}\tilde{Q}^2/g')^{\frac{1}{8}} t^{\frac{1}{8}} \quad \text{(plane)}, \tag{10a}$$

$$R \sim (g'Q^2/\nu^{\frac{1}{2}})^{\frac{1}{6}} t^{\frac{7}{12}}, \quad h_0 \sim (\nu^{\frac{1}{2}}Q/g')^{\frac{1}{3}} t^{-\frac{1}{6}} \quad \text{(axisymmetric)}. \tag{10b}$$

The equivalent relations for the *bottom current* (from (3) and (7)) are

$$L \sim (g'\tilde{Q}^3/\nu)^{\frac{1}{5}} t^{\frac{4}{5}}, \quad h_0 \sim (\nu\tilde{Q}^2/g')^{\frac{1}{5}} t^{\frac{1}{5}} \quad \text{(plane)}, \tag{11a}$$

$$R \sim (g'Q^3/\nu)^{\frac{1}{5}} t^{\frac{1}{2}}, \quad h_0 \sim (\nu Q/g')^{\frac{1}{4}} \quad \text{(axisymmetric)}. \tag{11b}$$

So far we have considered an ambient fluid of constant density only. In nature more often the ambient fluid is stratified, and thus it is of some interest to consider the spreading over or beneath a linearly stratified ambient fluid with density $\rho_a(z) = \rho_0(1 + \beta z)$, where ρ_s and ρ_b are the densities at the surface and bottom respectively. For current fluid $\rho_1 < \rho_s$ or $\rho_1 > \rho_b$ the driving density difference is a function of depth. It can be considered constant, however, if the ambient-density variation $\delta\rho_a = |\rho_0 - \rho_a(h)|$ across the current depth is small compared with $\Delta\rho$. Thus for $\delta\rho_a \ll \Delta\rho$ the driving gravity force is again given by (3), and the spreading relations are expected to be valid for stratified fluid under these conditions.

In the following paragraphs we will show how these spreading relations for the

† We would like to thank Dr H. E. Huppert for this suggestion.

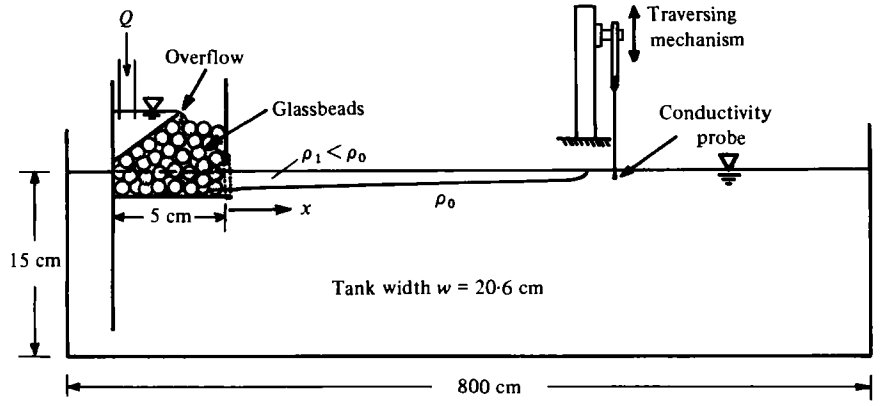

FIGURE 3. Tank and flow injector for plane surface gravity currents.

gravity–viscous regime correspond to our measurements of surface currents in a plane and axisymmetric geometry. In addition some axisymmetric bottom-current experiments were performed to clarify the dependence on the boundary conditions.

3. Apparatus and experimental procedure

The plane-surface-current experiments were performed in an 8 m long Plexiglas tank of 20·6 cm width (figure 3). The tank was filled to a height of 15 cm with salt water of specific density ρ_0 between 1·005 and 1·025. The current fluid of density $\rho_1 < \rho_0$ (mostly fresh water) was supplied from a static head tank. For flow visualization food colour was added to the injected fluid. The flow rate Q, measured with a rotameter, was manually controlled by a valve and held constant during each run. At one end of the tank the fluid was released through a flow injector at the surface of the ambient fluid at rest. The horizontal overflow and the closely packed glass beads in the injector improved the spanwise homogeneity of the inflow. The propagation of the front was measured as a function of time by taking a series of photographs through a scaled grid on the sidewall of the tank together with a clock, which was started at the same time as the flow. Some experiments with a reduced channel width were performed by inserting a vertical Plexiglas partition into the tank and blocking part of the flow injector.

The spreading of axisymmetric density fronts was studied in a square tank with 245 cm sides, as shown in figure 4. The ambient fluid of depth H between 7 cm and 15 cm was either salt water or constant density ρ_0 or linearly stratified salt water with density distribution $\rho(z) = \rho_0(1+\beta z)$, where $\beta = \rho_0^{-1}\partial\rho/\partial z < 0$. The linear stratification was set up by a method reported in Maxworthy & Browand (1975). Owing to the impermeability of the bottom and surface to salt diffusion the density gradient had to be zero at each boundary. The depth of bottom and surface layers of almost constant density was between 1 cm and 2 cm at the time the current was started (usually about 10 h after tank filling). Dyed fluid of density ρ_1 was then released from one corner of the tank at a constant flow rate $Q^* = \frac{1}{4}Q$ and spread radially into the 90° sector (Q is the flow rate into a 360° circle). To achieve a regular axisymmetric inflow the flow injectors shown in figure 4 were used for surface and bottom currents respectively. The front propagation was observed by photographing the tank and a clock timer at arbitrary time intervals from a height of 4 m above the tank.

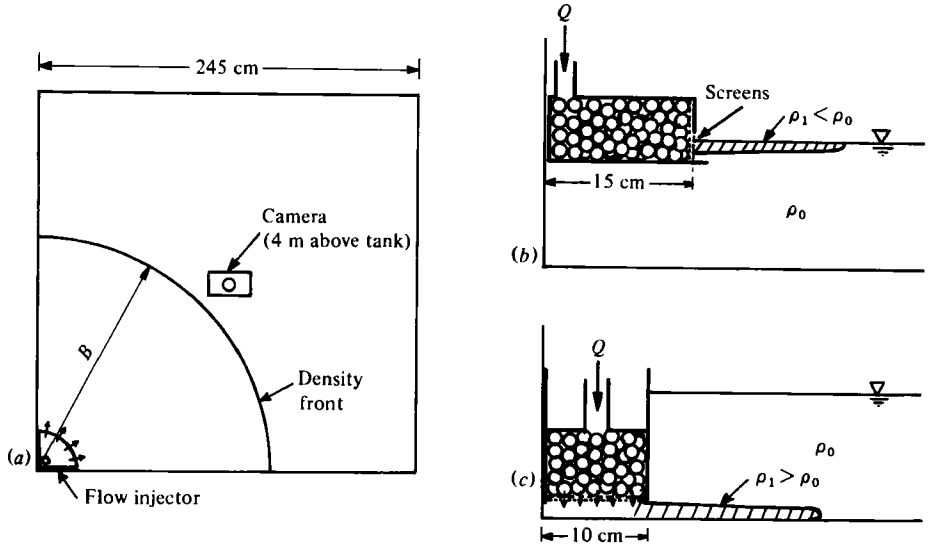

FIGURE 4. Tank for axisymmetric gravity currents. Plan view (*a*) and radial cross-section of 90° flow injectors for surface current (*b*) and bottom current (*c*).

For some runs the front line was not exactly circular, that is the radius R was a function of the azimuth, either because of asymmetric inflow conditions or a slow motion of the ambient fluid, which sometimes persisted for more than 10 h after the tank filling. In this case the current radius R was averaged, and data were used only from runs with a deviation from the circular shape of less than 10%. Flow perturbations at the surface-current front introduced artificially by local wind stress at the surface were observed to develop in a manner similar to that observed in the absence of the gravity current. The deformation of the current front was eventually smoothed out as the current front progressed.

In some cases density measurements were performed using a calibrated conductivity probe. Vertical density profiles were measured by slowly driving the probe through the fluid by means of a traversing mechanism. The probe speed was 0·3 cm/s, as compared with current velocities of the order of 1 cm/s. Also, density variations in time were recorded during the propagation of the density front across the probe at a fixed position. From the displacement of dyelines, produced by dropping small crystals of potassium permanganate from the water surface, crude vertical velocity profiles could also be observed.

4. Results and discussion

4.1. *Plane gravity currents*

In figure 5 we present a plot of the length of surface currents versus time for several combinations of the flow parameters $\tilde{Q}$ and g'. In order to keep the graph clear only 9 out of the 12 runs listed in table 1 are plotted here. For the parameters chosen, inertial forces are important only for a short period after the flow is started. The transition time $t_1 = \tilde{Q}^{\frac{1}{3}} g'^{-\frac{1}{3}} \nu^{-1}$ at which viscous forces overcome inertia forces is also given in table 1. For $t > t_1$, the logarithmic plot figure 5 represents the gravity–viscous regime for which the driving gravity force is balanced by the viscous drag. For all

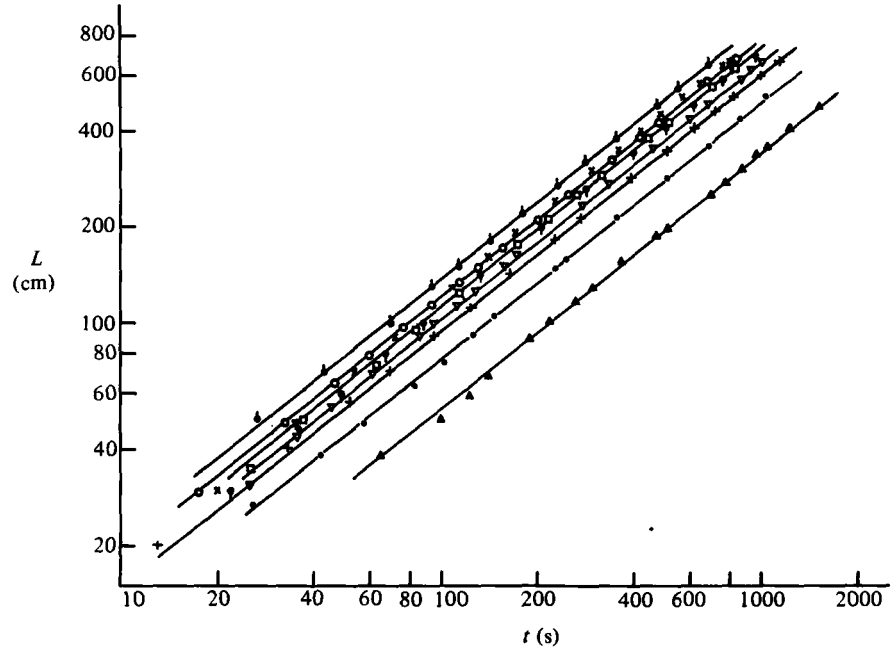

FIGURE 5. Length L of the plane surface gravity current versus time. (for symbols see table 1).

Q (cm²/s)	g' (cm/s²)	w (cm)	t_1 (s)	k_1'	
0·37	5·0	20·6	9·1	0·70	▲
0·66	4·2	20·6	22·1	0·74	●
0·60	25·0	20·6	5·9	0·74	▽
1·02	12·0	20·6	19·6	0·71	○
1·23	5·2	20·6	43·9	0·71	□
0·45	22·6	17·9	4·3	0·80	+
0·99	18·5	15·3	14·1	0·74	●
1·27	4·4	15·3	51·2	0·73	
0·72	9·9	12·8	14·0	0·78	
0·72	9·9	7·5	14·0	0·72	
0·96	18·5	5·0	13·5	0·72	×
1·31	4·4	5·0	53·4	0·71	●

TABLE 1. Parameters of plane-surface-current experiments: t_1 is the transition time ($9a$), w is the channel width, k_1' is the proportionality factor of the spreading relation (12) (the prime indicates results from experiments in a finite width channel); symbols refer to figures 5 and 6

runs the slope of the straight lines indicates a time dependence $L \sim t^{0.8}$. Curiously, this result is in very good agreement with the spreading relation ($11a$) derived for a bottom current with the no-slip boundary condition $u(z = 0) = 0$, and not with that derived for a current with a stress-free surface as one might first expect!

The velocity profiles $u(z)$ obtained by the displacement of vertical dyelines help to clarify the above result. Although we could not obtain quantitatively reliable results, since the falling crystals induced vertical velocities, qualitative information on the velocity distribution was obtained. Within the surface current the velocity

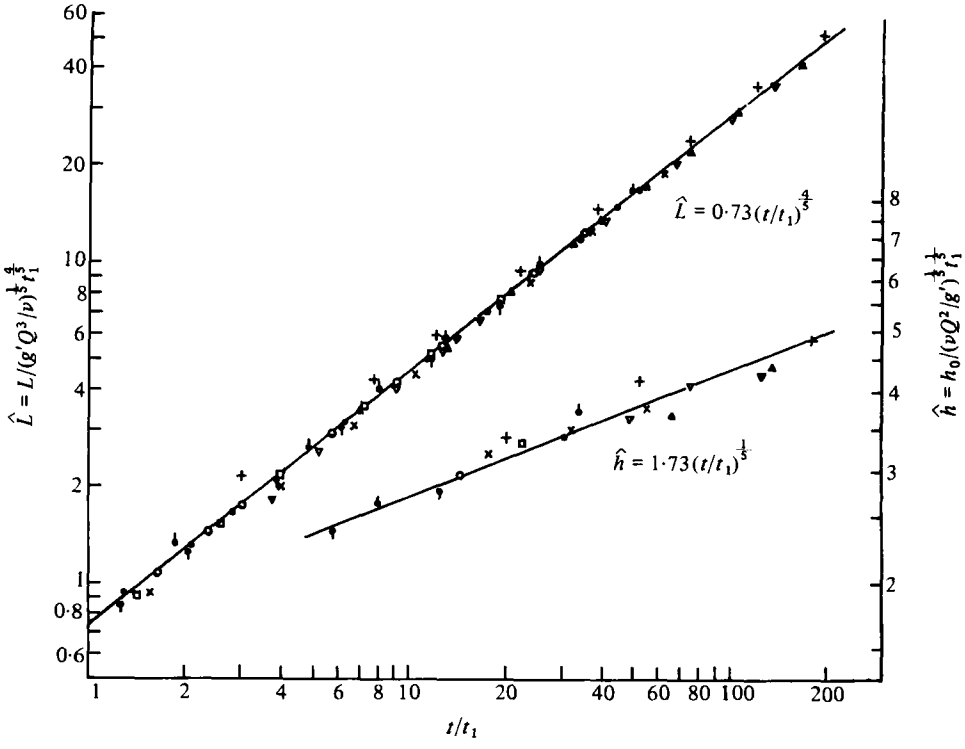

FIGURE 6. Dimensionless length $\hat{L}$ and thickness $\hat{h}$ of surface gravity currents versus t/t_1 (t_1 = transition time (9a)). For symbols see table 1.

increased from $u = 0$ at the surface to a maximum value at a depth close to the interface. Thus, in our experiments the surface was at rest and the flow was in fact equivalent to a bottom current. The agreement of the spreading relation (11a) with our measurements indicates that the velocity gradient at the surface was scaled with the current thickness h_0, and accordingly the viscous drag was determined by the surface stress $\tau_s \sim \mu U/h_0$. The no-slip condition at the surface was presumably due to the fact that small impurities in the water and from the surroundings formed a thin surface film, which acted like a solid boundary. A similar surface effect has been reported by Britter & Simpson (1978).

In order to check the dependence of the front spreading on the flow rate and the density difference, we rewrite (11a) in the form

$$\left.\begin{aligned} \hat{L} &= L[(g'\tilde{Q}^3/\nu)^{\frac{1}{5}}t_1^{\frac{4}{5}}]^{-1} = k_1(t/t_1)^{\frac{4}{5}}, \\ \hat{h} &= h_0[(\nu\tilde{Q}^2/g')^{\frac{1}{5}}t_1^{\frac{1}{5}}]^{-1} = k_2(t/t_1)^{\frac{1}{5}}. \end{aligned}\right\} \tag{12}$$

In the plot of the non-dimensional current length $\hat{L}$ *vs.* t/t_1 in figure 6 the data collapse fairly well onto a single line, indicating that the dependence of the spreading rate on the flow parameters $\tilde{Q}$ and g' is also well predicted by (12). The proportionality factor k_1' for the experiments in a finite-width channel is listed in table 1 for each run. For the mean value we find $k_1' = 0{\cdot}73$, with a standard deviation of 0·03.

The influence of sidewall stresses on the spreading rate was checked by performing several experiments with a reduced channel width. As argued in §2, owing to the side-

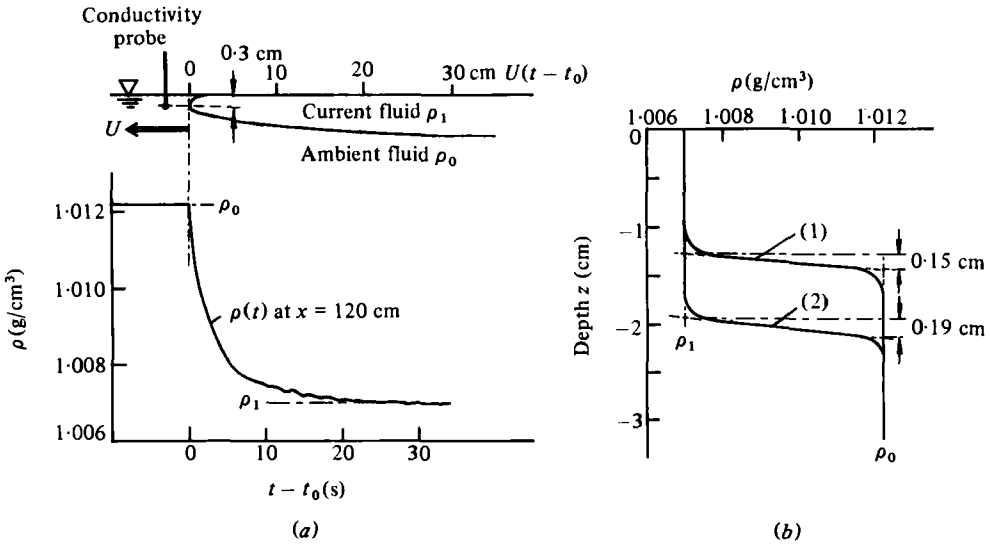

FIGURE 7. Density profiles of plane surface current ($\bar{Q}$ = 1·23 cm²/s, g' = 5·2 cm/s²), conductivity probe at x = 120 cm. (*a*) Density versus time at depth $z = -0{\cdot}3$ cm; front arrival time t_0 = 110 s. (*b*) Vertical density profiles at $x/L = 0{\cdot}63$, t = 190 s (1) and $x/L = 0{\cdot}23$, t = 670 s (2).

wall stress the viscous drag is increased by a factor $\alpha = 1 + 2ch_0^2/w(\nu t)^{\frac{1}{2}}$. In the spreading relation (12) this correction appears as a factor $\alpha^{-\frac{1}{4}}$, i.e. the proportionality factor for the spreading including sidewall stresses is $k_1' = \alpha^{-\frac{1}{4}}k_1$. An estimate of α at the beginning of the viscous regime gives an upper limit for the correction, since α decreases slightly with time. At $t = t_1 \sim h_0^2/\nu$ the correction is $\alpha^{-\frac{1}{4}} = (1 + 2h_0/w)^{-\frac{1}{4}}$, if we assume the constant of order unity to be $c = 1$. In our experiments we have $h_0(t_1) < 1$ cm, and thus $\alpha^{-\frac{1}{4}} < 0{\cdot}982$ and 0·935 for channel widths of w = 20·6 cm and 5 cm respectively. The factor k_1 for a current without side wall boundaries is therefore expected to be a few per cent higher than the measured value $k_1' = 0{\cdot}73$. Thus the agreement with the theoretical value $k_1 = 0{\cdot}804$ predicted in the accompanying paper by Huppert (1982) becomes more satisfactory, if side wall effects are taken into account. A definite dependence of k_1' on the channel width, however, could not be found from our measurements at $w/h_0 > 5$.

From visual observation the thickness h_0 of the dyed surface current at the injector nozzle could be measured with an accuracy of about 5 % (h_0 was of the order of 1 cm). A few data points were taken, and are also plotted in non-dimensional form in figure 6. The slight increase of the thickness h with time is in reasonable agreement with (12). The constant of proportionality determined by the straight line fitting the data is $k_2 = 1{\cdot}73$. Since the average thickness is $\bar{h} = Qt/L$, we find $\bar{h}/h_0 = (k_1k_2)^{-1} = 0{\cdot}79$.

The length of the frontal region where mixing is likely to have been important is defined by the region of strong horizontal density gradients, and was always small compared with the total length of the current. A typical time record of the density measured with the conductivity probe 0·3 cm below the surface is shown in figure 7 (*a*). Since the front velocity U is almost constant during the time interval shown, the density plot also represents the horizontal density profile at $z = -0{\cdot}3$ cm. The profile reveals a characteristic jump in the density gradient at the nose and a decreasing gradient behind the nose. Although some mixing was observed at the interface of the frontal region, a steep horizontal gradient is always maintained at the nose. Vertical

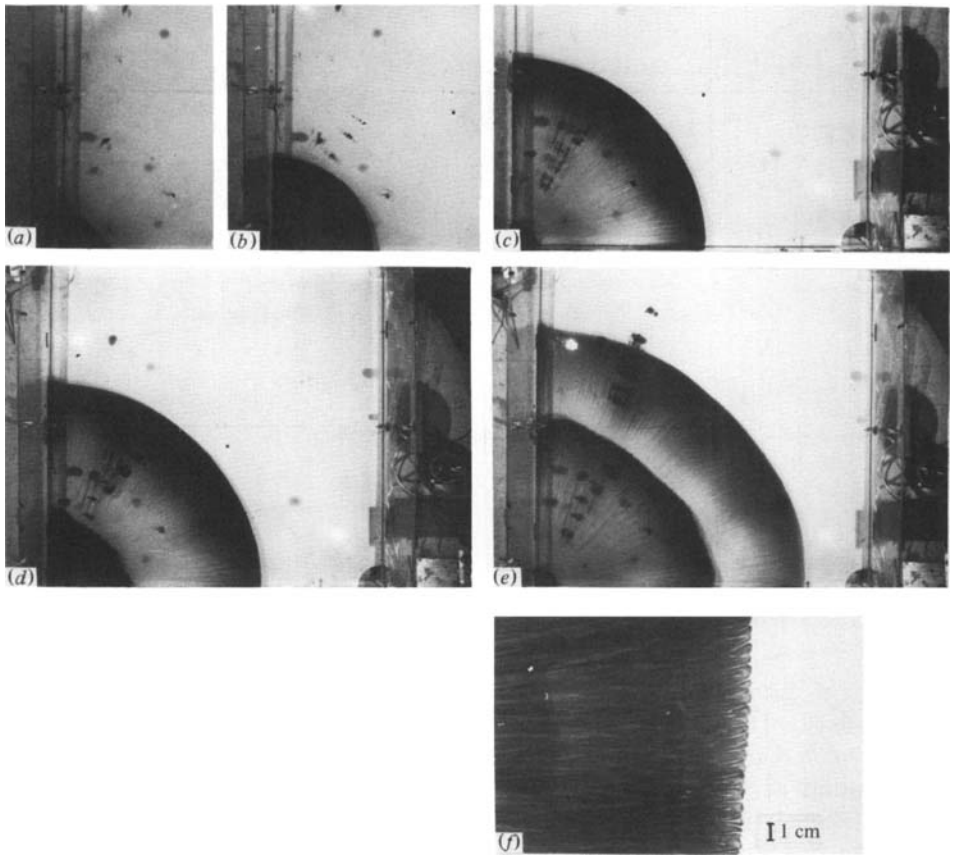

FIGURE 8. Plan view of axisymmetric surface current. Injected current fluid was dyed initially and dye was fed in again, before photograph (*d*) was taken. Photograph (*f*) shows details of the flow pattern at the front.

density profiles further behind the front region are shown in figure 7(*b*). Within the surface layer the density is constant and the interface is rather thin (typically between 10% and 20% of the current thickness h); hence vertical mixing and/or diffusion of salt is important only in this relatively narrow interfacial layer.

4.2. *Axisymmetric gravity currents*

A sequence of photographs of the axisymmetric surface current is shown in figure 8. The finite size of the tank had no obvious influence on the front propagation or the circular front shape until the distance between the front and the tank corner became less than about 30 cm, that is for $R > 220$ cm. As in the plane-current experiments the surface again was at rest (owing to a surface film) and thus our experiments correspond to a current with no-slip boundary condition.

A characteristic flow structure was observed at the front: figure 8(*f*) shows a regular pattern of lobes and clefts. This pattern has some resemblance to the structure observed by Simpson (1972) at the nose of bottom gravity currents in the gravity–inertia regime. As in the latter case the pattern is presumably due to a gravitational instability. Since the surface is at rest, light fluid of the current flows beneath heavier ambient fluid, which is trapped in the surface boundary layer. This

	Q (cm³/s)	g' (cm/s²)	t_1 (s)	β (10^{-3}/cm)	H (cm)	k	
(*a*) Surface current	19·3	2·8	26	2·4	9·1	0·61	
	19·3	2·9	26	0	11·9	0·63	⊙
	28	7·6	19	1·5	15·0	0·59	
	31	6·8	21	0	12·0	0·59	▲
	31	9·3	18	1·2	8·9	0·61	▽
	37	5·4	26	0	12·0	0·58	
	40	24·0	13	0	7·4	0·62	
	43	10·0	21	0	7·4	0·58	○
	43	11·0	20	1·7	7·2	0·62	
	43	11·4	19	0	8·0	0·62	
	49	5·3	30	1·7	7·6	0·60	
	55	3·3	41	1·2	8·6	0·58	
	55	8·8	25	0	7·7	0·58	□
	103	0·7	121	3·6	7·9	0·58	
	127	3·6	59	3·8	7·9	0·56	●
(*b*) Bottom current	31	7·5	20	0·8	9·2	0·60	●
	55	8·4	26	0·6	7·4	0·60	□
	75	18·0	20	0	10·8	0·61	○
	116	18·0	25	0	11·0	0·64	▲

TABLE 2. Parameters of axisymmetric experiments: t_1 is the transition time (9*b*), $\beta = (1/\rho_0)\,\partial\rho/\partial z$ is the stratification parameter; the factor of proportionality $k = R[(g'Q^3/\nu)^{\frac{1}{8}} t^{\frac{1}{4}}]^{-1}$ (11*b*) was determined from experiments; symbols refer to figures 9 and 10

unstable density stratification produces a convection pattern at the nose, which further behind the nose results in a streaky flow pattern.

The data for 15 axisymmetric surface currents have been reduced and are shown in table 2(*a*). The current radius R as a function of time is shown in figure 9. In order to keep the graph clear only 6 runs are plotted with parameter combinations Q, g' resulting in different current speeds. Since at small times the spreading depends on the initial conditions, a comparison with the asymptotic spreading relation for the gravity–inertia regime, terminated by the relatively short transition time t_1 (see table 2*a*), was not possible. On the other hand, because of the small transition time the spreading in the gravity–viscous regime became independent of the initial conditions of this regime when the current radius was still small enough to ensure accurate measurements of the viscous spreading within the size limits of the tank. Figure 9 shows that the time dependence of the current radius is $R \sim t^{\frac{1}{4}}$, in agreement with (11*b*) for a gravity current with no-slip boundary condition.

The dependence of the spreading rate on the flow rate Q and the reduced gravity g' is also well predicted by (11*b*): for the whole range of parameter variations shown in table 2(*a*) the proportionality factor was found to be constant ($k = 0{\cdot}60 \pm 0{\cdot}02$). The thickness h_0 of the surface current was typically between 0·5 cm and 1·5 cm, and the depth H of the ambient fluid between 7 cm and 15 cm. Up to the maximum depth ratio of $h_0/H \approx 0{\cdot}2$ the finite depth of the ambient fluid had no measurable effect on the spreading rate.

In order to confirm that the surface current with the no-slip boundary condition in our experiments is equivalent to a bottom current, we present some measurements of the spreading of three-dimensional bottom currents in figure 10 and table 2(*b*). For the gravity–viscous regime the logarithmic plot again shows the time dependence

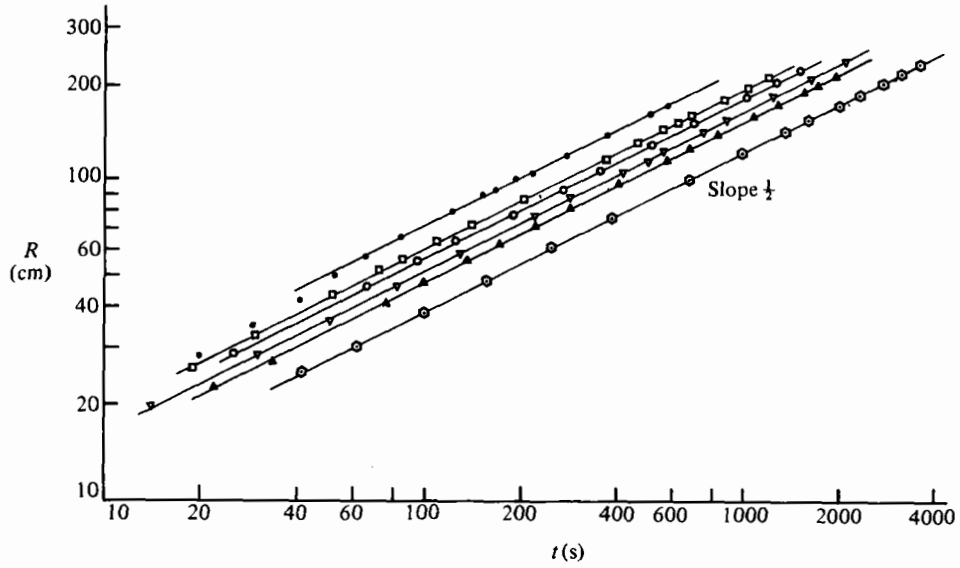

FIGURE 9. Radius R of axisymmetric surface gravity currents versus time for different parameters Q and g' (see symbols in table 2a).

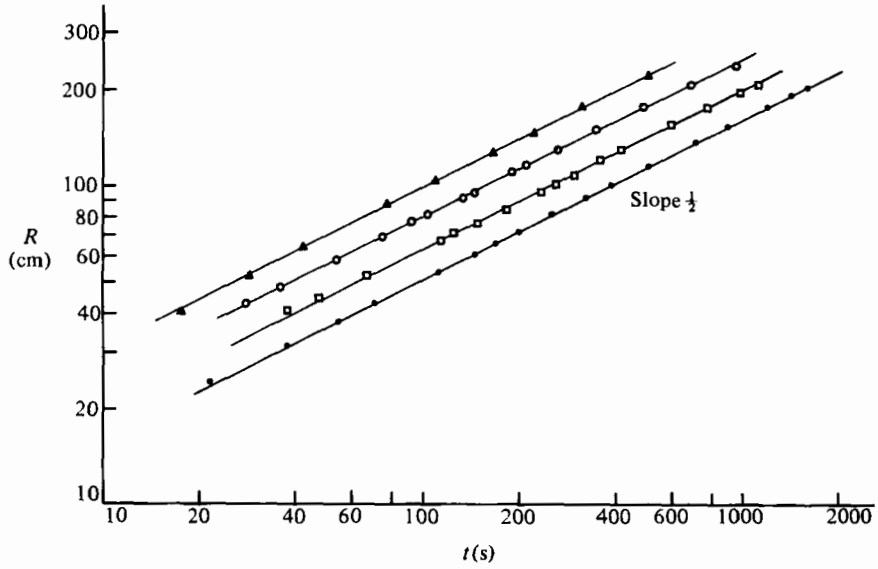

FIGURE 10. Radius R of axisymmetric bottom gravity currents versus time for different parameters Q and g' (see symbols in table 2b).

$R \sim t^{\frac{1}{2}}$, in agreement with (11b). Furthermore, the proportionality factor k (table 2b) agrees well with the value 0·60 measured for the surface current.

For surface fronts in the ocean a further vertical scale is introduced by the stratification in the thermocline. In some of our experiments we simulated the thermocline by a linear stratification $\rho_a(z) = \rho_0(1+\beta z)$ in the ambient fluid. The ambient density variation $\delta\rho_a$ across the current depth (Figure 11b) was always small compared with the density difference $\Delta\rho$ between both fluids. In §2 we argued that

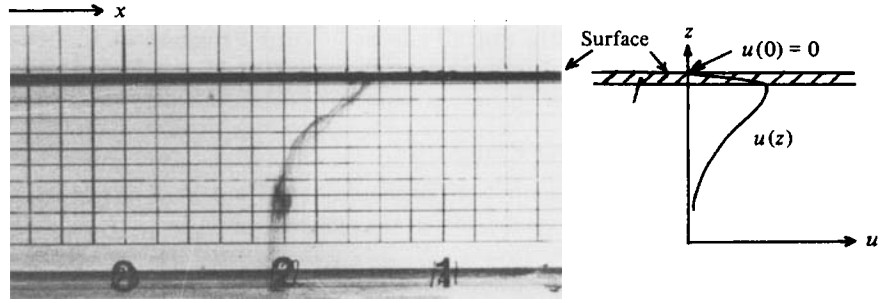

(*a*)

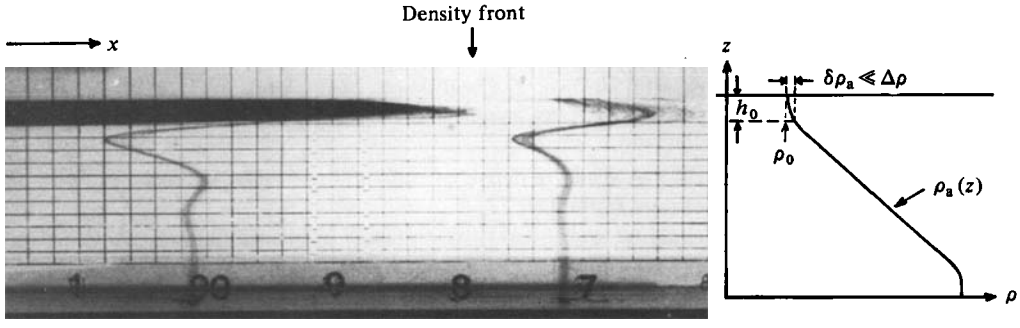

(*b*)

FIGURE 11. Vertical velocity profiles $u(z)$ of plane surface gravity currents above (*a*) homogeneous fluid and (*b*) above linear stratified fluid.

under this condition the same force balance is valid as for the constant density case. The spreading rate was indeed found to be independent of the stratification parameter β (table 2). The flow field in the stratified fluid, however, was different from that in the homogeneous ambient fluid. In figure 11 we show velocity profiles of currents above homogeneous and stratified fluids for comparison. (The photographs are taken from plane currents, since in this geometry better contrast was achieved for the dyeline visualization. For the axisymmetric flow the velocity profiles are qualitatively similar.) In the homogeneous case the velocity has a maximum value close to the interface, and the vertical shear at the surface at rest is large compared with the interfacial shear. Therefore the viscous drag only depends on the surface stress, in agreement with our analysis for a gravity current with no-slip boundary conditions. From our measurements we find the same spreading rate for the surface current above homogeneous fluid and stratified fluid. Thus, in the latter case the viscous drag is determined only by the surface shear stress, and the flow field in the ambient fluid (figure 11*b*) does not affect the overall force balance, but is simply a response to it. The characteristic velocity profile with alternations of the flow direction is a well-known feature of shear layers in stratified viscous flows, and such profiles have been observed in the upstream wake of bodies towed horizontally through stratified fluids (Browand & Winant 1972) and for gravity driven currents spreading at an equilibrium level in the interior of a stratified layer (Maxworthy 1972).

The authors wish to acknowledge the support of the Office of Naval Research through Contract no. N0014-76-C-0211 and of the Sea Grant Program at U.S.C. We also gratefully appreciate the help of our laboratory assistant Casey De Vries.

REFERENCES

BENJAMIN, T. B. 1968 Gravity currents and related phenomena. *J. Fluid Mech.* **31**, 209–248.

BRITTER, R. E. & SIMPSON, J. E. 1978 Experiments on the dynamics of a gravity current head. *J. Fluid Mech.* **88**, 223–240.

BROWAND, F. K. & WINANT, C. D. 1972 Blocking ahead of a cylinder moving in stratified fluid: an experiment. *Geophys. Fluid Dyn.* **4**, 29–53.

FAY, J. A. 1969 The spread of oil slicks on a calm sea. In *Oil on the Sea* (ed. D. P. Hoult), pp. 53–63.

GARVINE, R. W. & MONK, J. D. 1974 Frontal structure of a river plume. *J. Geophys. Res.* **79**, 2251–2259.

HOULT, D. P. 1972 Oil spreading on the sea. *Ann. Rev. Fluid Mech.* **4**, 341–368.

HUPPERT, H. E. 1982 The propagation of two-dimensional and axisymmetric viscous gravity currents over a rigid horizontal surface. *J. Fluid Mech.* **121**, 43–58.

HUPPERT, H. E. & SIMPSON, J. E. 1980 The slumping of gravity currents. *J. Fluid Mech.* **99**, 785–799.

KLEMAS, V. & POLIS, D. F. 1977 A study of density fronts and their effect on coastal pollutants. *Remote Sensing of Environment* **6**, 95–126.

MAXWORTHY, T. 1972 Experimental and theoretical studies of horizontal jets in a stratified fluid. In *Proc. Int. Symp. on Stratified Fluid, Novosibirsk*, no. 17.

MAXWORTHY, T. & BROWAND, F. K. 1975 Experiments in rotating and stratified flows: oceanographic application. *Ann. Rev. Fluid Mech.* **7**, 273–305.

MCGUIRK, J. J. & RODI, W. 1979 Mathematical modelling of three-dimensional heated surface jets. *J. Fluid Mech.* **95**, 609–633.

SIMPSON, J. E. 1972 Effects of the lower boundary on the head of a gravity current. *J. Fluid Mech.* **53**, 759–768.

SIMPSON, J. E., MANSFIELD, D. A. & MILFORD, J. R. 1977 Inland penetration of sea-breeze fronts. *Q. J. R. Met. Soc.* **103**, 47–76.